Silver–Carbon-Nanotube Metal Matrix Composites for Metal Contacts on Space Photovoltaic Cells

Omar K. Abudayyeh, Nathan D. Gapp, Cayla Nelson, David M. Wilt, *Member, IEEE*, and Sang M. Han, *Member, IEEE*

***Abstract*—In this paper, multiwalled carbon nanotubes are being investigated for mechanical reinforcement of metal contacts on inverted metamorphic multijunction solar cells. We have focused on a silver–carbon-nanotube layer-by-layer microstructure for this study. The silver layer is electrodeposited, and the carbon nanotube layer is deposited by various methods, including electrodeposition, nanospreading, and drop casting. To increase the adhesion strength to metal and achieve efficient metal nanotube stress transfer, carbon nanotubes are chemically functionalized with carboxylic or amine groups prior to deposition. The metal–carbon-nanotube composites are characterized mechanically and electrically through nanoindentation and strain failure tests. The strain failure tests show that the conductivity can be maintained up to 42-μm-wide microcracks in the composite layer, where the carbon nanotubes bridge the gap.**

***Index Terms*—Composite materials, metallization, photovoltaic cells.**

I. Introduction

THE advanced solar cells used in space vehicles today are rapidly moving toward thin-film-based inverted metamorphic multijunction (IMM) solar cells [1]–[3] mounted on flexible substrates. However, IMM cells are more prone to cracking than state-of-the-art triple junction cells. Cell cracking can lead to metal contact failure on IMM cells, compromising the power generation. Recently, Kajari-Schröder *et al.* [4] characterized microcracks in crystalline-silicon-based photovoltaic cells, using electroluminescence after artificial aging and snow damage (see Fig. 1). These microcracks can electrically disconnect areas of the cells and lead to substantial power loss ($\sim$16%) [5]. To mitigate the power loss and increase the lifetime of IMM cells, we have developed and investigated silver (Ag) metal films imbedded with multiwalled carbon nanotubes (CNTs), also known as metal matrix composites (MMCs), for the reinforced mechanical strength against stress-induced cracks [6].

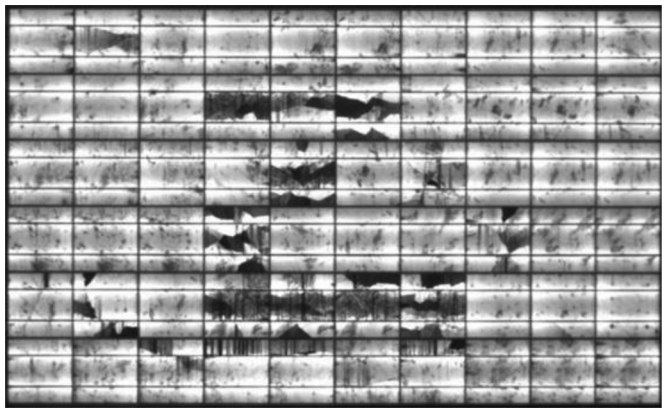

Fig. 1. Electroluminescence image of a microcracked photovoltaic module. Dark regions are electrically inactive areas [4].

Numerous techniques exist today to deposit MMCs, including the powder metallurgy route, the melting and solidification route, and the electrochemical route [7]. In our case, an electrochemical deposition method is chosen to readily control the MMC microstructure. One of the microstructures currently being explored is an Ag-CNT layer-by-layer (LBL) structure, in which functionalized CNTs are deposited on electroplated Ag in an alternating fashion. Here, we compare different CNT deposition techniques, including electrochemical deposition [8], [9], nanospreading [10], and drop casting.

In this investigation, we have primarily focused on 1) optimization of a cyanide-free electrochemical deposition of Ag, 2) surface functionalization of CNTs to make their surface more hydrophilic and wetting to metals, 3) control of CNT incorporation in the LBL microstructure using different deposition methods, and 4) mechanical and electrical characterization of the composite films. Currently, we are able to deposit lustrous-mirror-finish Ag films, using a commercial Ag-plating solution with precise control of current density. We observe that the carboxylation of CNTs produces a stable homogeneous suspension of negatively charged carbon nanotubes at pH 6. One of the microstructures being explored is an Ag-CNT LBL structure, where the surface coverage of CNTs is the main variable that directly affects the CNT packing fraction and metal intercalation through the CNT network. We quantify the CNT surface coverage as a function of different deposition variables by digitally analyzing scanning electron microscopy images. We further analyze how this surface coverage correlates with the mechanical and electrical properties of the MMC films. We characterize the mechanical properties using nanoindentation and strain failure tests.

Manuscript received June 1, 2015; revised August 18, 2015; accepted September 14, 2015. Date of publication October 1, 2015; date of current version December 18, 2015. This work was supported in part by the Air Force Research Laboratory under Grant FA9453-14-1-0242.

O. K. Abudayyeh, C. Nelson, and S. M. Han are with the Chemical and Biological Engineering Department and NanoScience and MicroSystems, University of New Mexico, Albuquerque, NM 87131 USA (e-mail: odayyeh@unm.edu; cmnelson@unm.edu; meister@unm.edu).

N. D. Gapp and D. M. Wilt are with the Air Force Research Laboratory, Kirtland AFB, Albuquerque, NM 87117 USA (e-mail: nathan.gapp@us.af.mil; david.wilt@kirtland.af.mil).

Color versions of one or more of the figures in this paper are available online at http://ieeexplore.ieee.org.

Digital Object Identifier 10.1109/JPHOTOV.2015.2480224

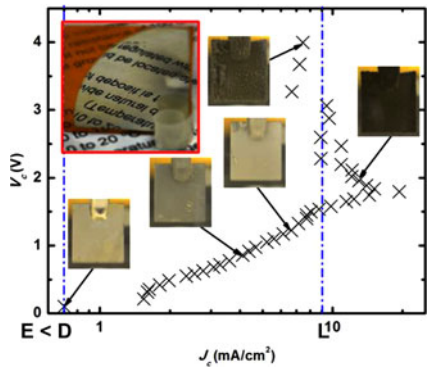

Fig. 2. Cathode potential V_c versus cathode current density J_c. The region between Point D and Point L defines the ideal operating window where the finish of plated Ag is bright.

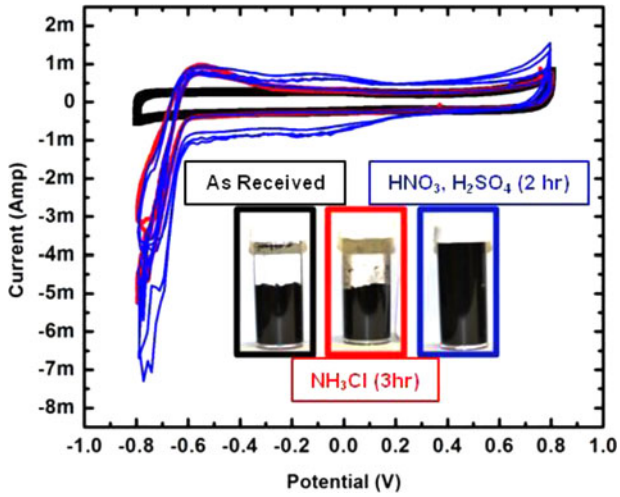

Fig. 3. Cyclic voltammetry measurements on the as-received (black), amine-terminated (red), and carboxylated (blue) CNTs with corresponding images of the CNTs solutions.

II. Experimental Methods and Results

A. Silver Electroplating

Silver electroplating is typically performed in cyanide-based aqueous solutions because these processes offer most the consistent deposition qualities at a low cost [11]. However, due to their toxicity and environmental concerns, finding suitable noncyanide-based electrolyte solutions is highly desired to replace toxic cyanide processes [12]–[14]. In this effort, we have successfully developed and optimized an electrochemical Ag deposition using a commercially available plating solution, E-brite 50/50 RTP, through the manipulation of key parameters such as pH, temperature, ionic strength, and current density. Plating conditions are optimized in a series of experiments. The main variable is cathodic current density J_c, while Ag ion concentration, pH, and bath temperature are held constant. Fig. 2 shows the cathode potential V_c versus current density J_c with corresponding images of Ag electroplated on GaAs substrates. Point E is below 0.6 mA/cm^2 in our case, where no current is flowing at the equilibrium potential. Point D demarcates the decomposition potential where the electrode reaction begins, and Ag starts to deposit. Point L defines the limiting current density, above which Ag deposition is transport limited, V_c becomes very unstable, and the plated Ag becomes "spongy." The region between D and L defines the ideal operating window where the plated Ag appears bright, which is associated with the high-quality metal finish. Note that the uppermost sample in Fig. 2, despite its location in the ideal window of operation, appears dark/"spongy", where the control set point on current density is well above 10 mA/cm^2, and the control over J_c becomes unstable. A current density of 3 mA/cm^2 consistently results in a bright finish; therefore, this current density is used in all subsequent Ag electrodepositions.

In addition to precise control over the operating current density, we observe that the initial seeding layer on the substrate significantly affects the final film quality. Various thin ($\sim$100 nm) seeding layers are explored, including sputter-coated Ti, sputter-coated Ag, and Ag deposited by physical vapor deposition (PVD). The PVD Ag seeding layer and subsequent electroplating of Ag result in a mirror finish (see the upper left inset of Fig. 2). That is, mirror finishes are obtained through the precise control of current density and the use of appropriate seeding layer.

B. Carbon Nanotube Functionalization

The high mechanical strength and good electrical/thermal conductivities of CNTs [15], [16] make them a suitable component in the MMC to reinforce the metal gridlines. For this paper, we have focused on low-purity multiwalled CNTs as they offer lower cost and longer lengths than single-walled CNTs. However, in order to harness these properties, CNTs have to be properly imbedded within the metal matrix. One common approach to incorporate CNTs in the metal matrix is through chemical functionalization, which allows for chemical bonding between CNTs and their surrounding environment [17]–[20]. In order to enhance the wettability and adhesion of CNTs to metal, two groups of surface-functionalized CNTs are developed. The first group is functionalized with COOH for negative surface charge, following a standard acid reflux method [21], [22]. The maximum electrokinetic mobility of CNTs is achieved through an acid treatment in a 1:3 HNO_3:H_2SO_4 mixture [22]. The second group is functionalized with NH_2 for positive surface charge by sonicating CNTs in 2.8-M NH_4Cl aqueous solution. Carboxylation of CNTs produces stable homogenous aqueous solutions of CNTs, as seen in Fig. 3. Cyclic voltammetry tests are performed on the as-received, NH_2-functionalized, and COOH-functionalized CNTs. We observe the highest overall integrated charge (see the blue line in Fig. 3) associated with the carboxylated CNTs, which indicates that carboxylated CNTs assume the highest amount of surface charge and presumably the highest electrokinetic mobility compared with neutral and amine-terminated CNTs.

C. Carbon Nanotube Deposition Methods

For microstructural comparison, COOH-terminated CNTs are used to create an LBL Ag composite microstructure. First,

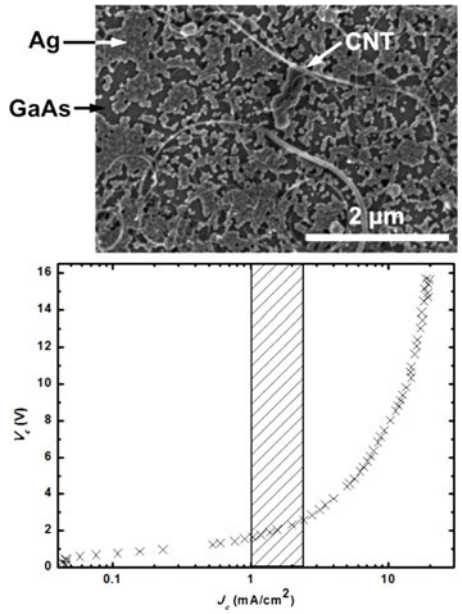

Fig. 4. (Top) SEM image of COOH-terminated CNTs deposited on 40-nm-thick sputter-coated Ag to clearly show Ag dissolution during negatively charged CNT deposition on positively biased working electrode. (Bottom) *I–V* characteristic curve. Shaded region indicates the optimum operating range above which V_c rapidly rises with increasing J_c.

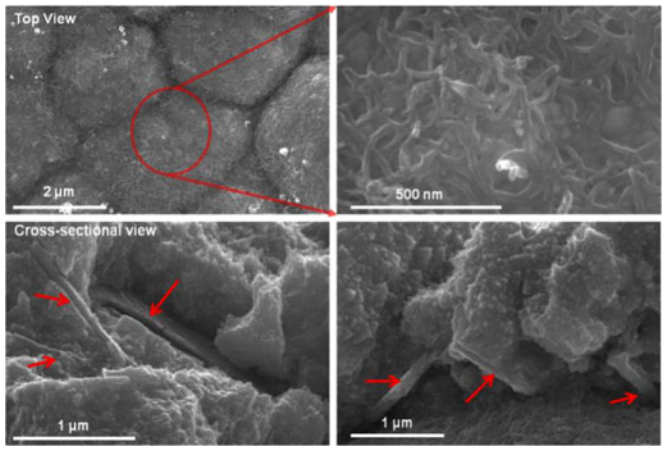

Fig. 5. (Top) SEM images of COOH-terminated CNTs deposited on electroplated Ag, using the nanospreader technique. Five successive layers of CNTs are deposited at a blade pull speed of 10 μm/s. (Bottom) Cross-sectional SEM images of Ag-CNT-Ag composite structure. The CNTs, indicated by red arrows, exhibit good adhesion to the surrounding Ag matrix.

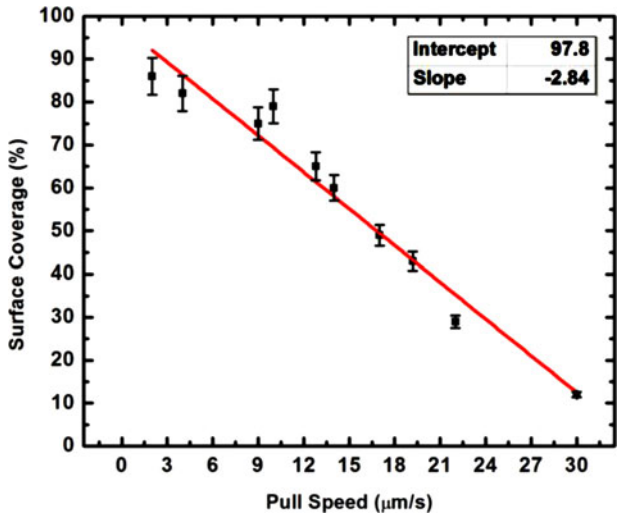

Fig. 6. Linear relation between the pull speed and corresponding surface coverage of CNTs using the nanospreader method.

a 2-μm-thick Ag film is electroplated on GaAs followed by electrochemical deposition of CNT-COOH at –0.5 mA/cm^2 for 15 min. The sample is then electroplated with another 2-μm-thick Ag layer. Due to the negative surface charge on CNT-COOH, a positive bias must be applied to the working electrode (i.e., anode) to deposit CNTs. Consequently, the plated Ag dissolves back into the solution during CNT deposition (see Fig. 4).

As an alternate method to electrochemical deposition, functionalized CNTs are deposited using a nanospreader technique. A 2-μm-thick Ag layer is first electroplated on a 100-nm-thick PVD Ag seeding layer on GaAs samples. The nanospreader technique [10] is then used to deposit a thin layer of CNTs by dragging at a constant velocity the meniscus of microliter suspension droplets of CNTs trapped between the substrate and a moving Teflon blade. Five layers of carboxylated CNTs are successively deposited at a blade pull speed of 10 μm/s. The samples are then plated with another 2-μm-thick Ag layer, creating an MMC film with a total thickness of $\sim$4 μm. Fig. 5 shows the nanospreader sample before the second Ag layer is deposited (top SEM images), and a cross-sectional view after the second Ag layer is deposited (bottom SEM images). The cross-sectional SEM images show CNTs intercalating the Ag matrix. These images suggest that the surface functionalized CNTs adhere well to Ag and that these CNTs would bridge the microcracks that are formed on strain-induced failure.

A range of deposition rates is investigated using the nanospreader technique with pull speeds ranging from 2 to 30 μm/s and droplet volumes ranging from 10 to 50 μL. Through the manipulation of pull speed, we are able to obtain CNT surface coverage ranging from 12% to 86% (see Fig. 6). Here, we define the surface coverage as the percentage of substrate surface covered by CNTs, ignoring any CNT overlap. The corresponding surface coverage is quantified through the digital image processing of SEM images. Using ImageJ program, the SEM images are converted into a matrix of gray-scale values with the corresponding *xy* coordinates. The gray-scale values are then plotted in a histogram, and a cutoff gray value is assigned per image. This cutoff value represents the gray-scale value of an open space; hence, all gray values less than this cutoff value are counted and divided by the total counts, giving the percentage surface coverage. We note that this cutoff value is not a constant due to the variability in contrast and brightness settings from image to image.

While the nanospreader technique offers precise control over the CNT surface coverage, the slow throughput limits its manufacturability. As an alternative method of deposition, we have

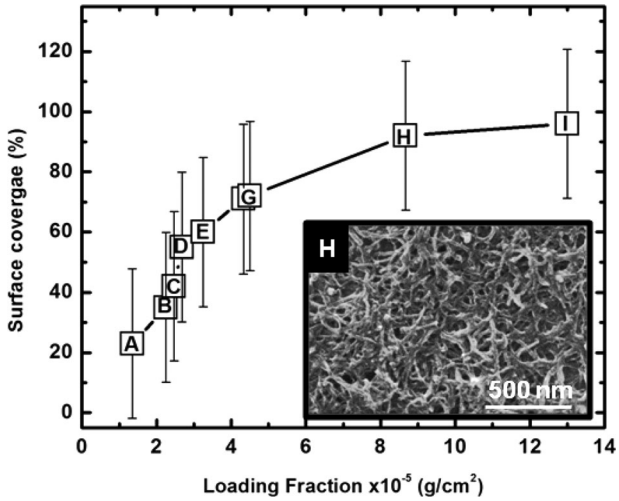

Fig. 7. CNTs loading fraction versus surface coverage with standard deviation bars. Past point H (> 9 g/cm^2), the surface coverage plateaus, asymptotically approaching 100%.

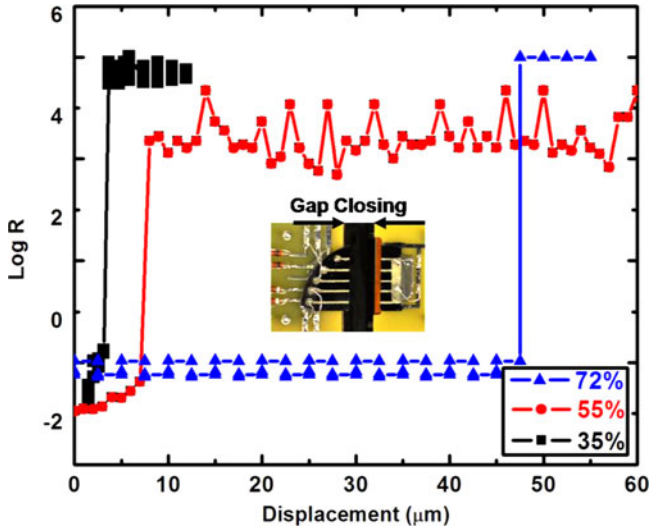

Fig. 8. Log plot of resistance versus gap across fractured MMC gridlines with three different CNT surface coverages. The connection is reestablished at 49, 9, and 5 μm for samples with CNT surface coverage of 72%, 55%, and 35%, respectively.

also applied a simple drop casting method, using a solution of carboxylated CNTs. We explore a range of different CNT loading fractions (i.e., CNT solution concentration) and digitally analyze the subsequent surface coverage (see Fig. 7 inset). Digital analysis is performed using ImageJ program. Fig. 7 shows how the CNT loading fraction translates to the percentage surface coverage. We use different CNT loading fractions to prepare MMC gridlines (each 1-mm wide) to create the LBL microstructure. First, a 2-μm-thick Ag film is electroplated on a 100-nm-thick PVD Ag seeding layer on an InP substrate. The solution of CNT-COOH is then drop-cast at room temperature. Another 2-μm-thick Ag layer is finally electroplated on top.

D. Electrical and Mechanical Characterization

Using a four-point probe, we measure the sheet resistance (thus conductivity) of 2-μm-thick Ag and then of the complete MMC composite layer after drop casting 600 μL of CNT solution (2.2×10^{-4} g_{CNT}/cm^2) and plating the final 2-μm-thick Ag layer. Nine measurements are taken for each layer. The initial Ag layer shows $1.2 \times 10^5/\Omega\cdot$cm conductivity. After applying the CNT layer and growing the second Ag layer, the complete stack shows $3.0 \times 10^5/\Omega\cdot$cm conductivity. Despite using low-purity multiwalled CNTs, a higher conductivity ($3.0 \times 10^5/\Omega\cdot$cm) is observed for the complete MMC compared to pure silver ($1.2 \times 10^5/\Omega\cdot$cm), emphasizing the excellent electrical properties of CNTs and their good adhesion to the Ag matrix.

A strain failure test is performed to determine how well the MMC samples can maintain the electrical conductivity upon mechanical fracture. A set of four parallel MMC gridlines, deposited on an InP substrate, are first mounted on two printed circuit boards using an adhesive (see the insets of Figs. 8 and 9). Upon curing the adhesive, the substrate is scribed with a diamond tip to generate a crack that propagates across the substrate backside, orthogonal in direction to the MMC gridlines. The cracked substrate is then attached to a linear stage controlled by a

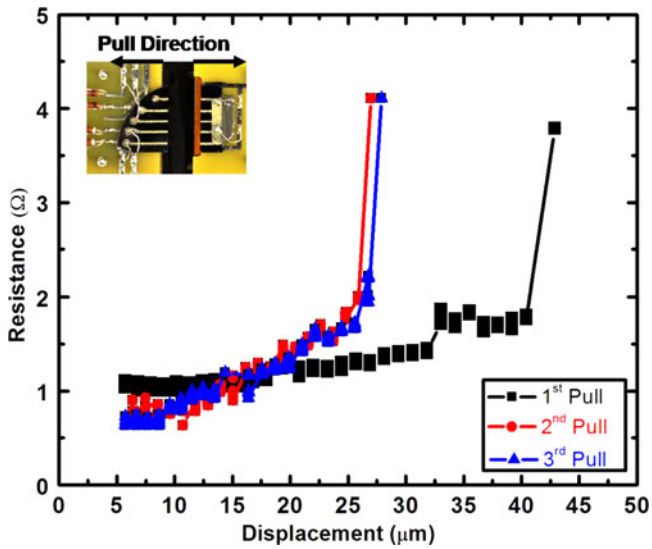

Fig. 9. Strain failure test of a MMC gridline (96% CNT surface coverage using drop cast method). The maximum gap at which the electrical connection is lost is reduced by $\sim$34% after the second pull test but remained constant after subsequent pull tests.

stepper motor. The resistance across each of the MMC gridlines is continuously recorded as the gridlines are pulled apart at micrometer increments until the electrical resistivity approaches infinity upon plastic failure. Following the first electrical disconnect, the gap is incrementally closed in reverse until the electrical connection is reestablished across the gridlines (see Fig. 8); the substrate is then pulled apart again. This process is repeated until no further change is seen in the gap width at which the connection is lost. Fig. 9 shows a pull test of an MMC gridline with 96% CNT coverage. After the second pull test, the maximum gap at which the electrical connection is lost is reduced by $\sim$34% but subsequently remained constant with

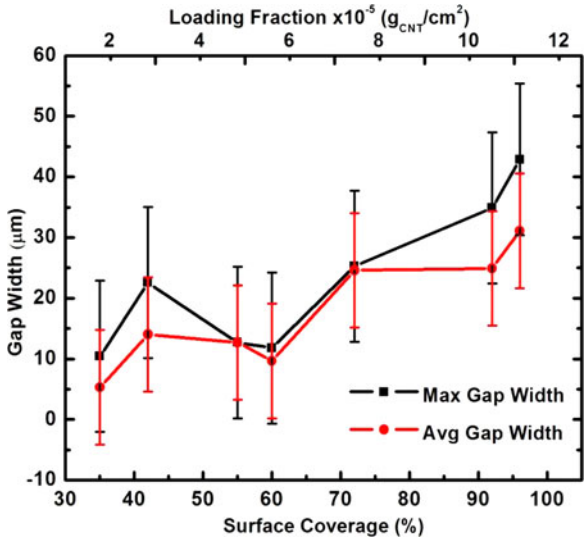

Fig. 10. Maximum and average gap widths achieved before lost connection as a function of CNT surface coverage and loading fraction.

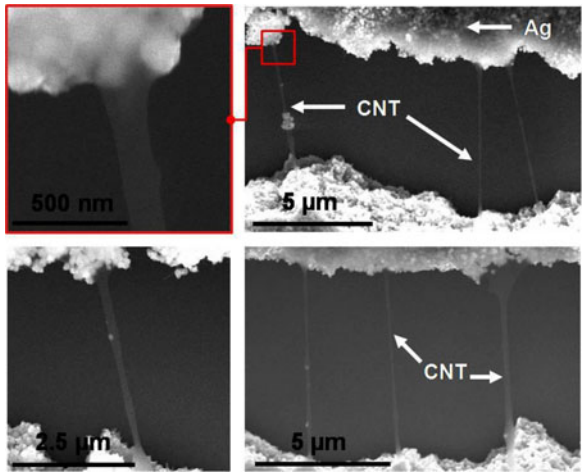

Fig. 11. SEM images of CNTs anchored in Ag layers clearly showing CNTs bridging cracks up to 9-μm wide.

additional pull tests. Using the drop casting method, a set of MMC samples is prepared with different CNT surface coverage. The MMC gridlines are assessed, using the strain failure test. Four gridlines with the same CNT loading are tested, and the maximum and average gaps before the loss of electrical connection are recorded in Fig. 10. The pull tests reveal that the electrical connection is maintained across larger gaps with higher CNT surface coverage, reaching a maximum of 42-μm-wide gap. As the CNT surface coverage increases from 35% to 96%, we observe a monotonic increase in the average gap. Electroplated Ag lines without CNTs are also analyzed as control, using the strain failure test. Unlike MMC films, the Ag gridlines did not withstand the initial crack generated on the substrate ($\sim$4-μm wide), and the electrical connection is immediately and irrecoverably lost.

It is clearly evident that the incorporation of CNTs within the Ag matrix enhances the electrical conductivity of metal lines upon fracture. To visualize this capability, we intentionally fracture an MMC film and examine the cracks under SEM. We observe the CNTs of various lengths bridging gaps ranging from 0.2 to 9 μm. The CNTs are anchored in the Ag matrix, indicating a good adhesion between the functionalized CNTs and the Ag matrix (see Fig. 11). A typical current density through an MMC gridline under our testing is approximately 750 A/cm^2 before fracture. Once the crack is generated, the total current (30 mA) is conducted through only a limited number of CNTs at the fracture point, as shown in Fig. 11. We have not measured the maximum current density that MMCs can tolerate after fracture yet, but we project that by varying the CNT loading, it would be possible to conduct a realistic amount of current typical of space photovoltaic cells.

Mechanical characterization is performed on the MMC films and plated silver films with no CNTs (baseline) using a Berkovich round tip nanoindenter. Stress–strain curves are obtained at a depth profile of 2 μm. MMC samples of 4-μm thickness are prepared using nanospreader and drop casting methods to deposit CNTs at various loading fractions. The nanoindentation analysis reveals that the composite film has a lower elastic modulus (10 GPa) than pure silver (73 GPa) [23], which is contrary to our initial prediction given the high elastic modulus of CNTs (1000 GPa) [24]. Nanoindentation tests performed on bare electroplated Ag result in hardness values < 1 GPa, much lower than the reported literature values of Ag. The lower elastic modulus is attributed to the electroplating process of silver, in which hydrogen is incorporated and trapped within the composite. Our finite-element analysis also corroborates this speculation, where the elastic modulus near 10 GPa is predicted with approximately 4% void fraction. While the composite elastic modulus is lower than that of pure silver, the strain failure tests show that the carbon nanotubes can bridge 10–42-μm-wide microcracks, maintaining electrical conductivity. We are currently investigating how hydrogen incorporation within electroplated silver affects hardness and elastic modulus, and we will report the study in a future publication.

III. Conclusion

In this study, we have developed and characterized Ag-CNT MMC films that maintain electrical conductivity upon mechanical fracture of the substrate. Our composite lines are capable of bridging cracks in the underlying semiconductor substrates up to 42 μm. That is, the incorporation of CNTs within the Ag matrix renders the metal lines more resilient against mechanical failures, compared to the 100% Ag lines. In addition to maintain the electrical conductivity over the stress-induced cracks, the composite films can reestablish the electrical connection when the cracks close up. This "self-healing" behavior of MMC gridlines is an important characteristic in light of the extreme temperature fluctuations encountered in space operations, in which the photovoltaic cells undergo constant expansion and contraction.

References

[1] A. Cornfeld *et al.*, "Development of a four sub-cell, inverted metamorphic multi-junction (IMM) highly efficient AM0 solar cell," in *Proc. IEEE 35th Photovoltaic Spec. Conf.*, Honolulu, HI, USA, 2010, pp. 000105–000109.

[2] P. Patel *et al.*, "Experimental results from performance improvement and radiation hardening of inverted metamorphic multijunction solar cells," *IEEE J. Photovoltaics*, vol. 2, no. 3, pp. 377–381, Jul. 2012.
[3] J. Boisvert *et al.*, "High efficiency inverted metamorphic (IMM) solar cells," in *Proc. IEEE 39th Photovoltaic Spec. Conf.*, Tampa, FL, USA, 2013, pp. 2790–2792.
[4] S. Kajari-Schröder, I. Kunze, U. Eitner, and M. Köntges, "Spatial and orientational distribution of cracks in crystalline photovoltaic modules generated by mechanical load tests," *Sol. Energy Mater. Sol. Cells*, vol. 95, pp. 3054–3059, 2011.
[5] M. Köntges, I. Kunze, S. Kajari-Schröder, X. Breitenmoser, and B. Bjrneklett, "The risk of power loss in crystalline silicon based photovoltaic modules due to microcracks," *Sol. Energy Mater. Sol. Cells*, vol. 95, pp. 1131–1137, 2011.
[6] J. T. H. Tsai and H. L. Hwang, "Carbon nanotube reinforced conductors for flexible electronics," *J. Display Technol.*, vol. 5, pp. 232–235, 2009.
[7] S. R. Bakshi, D. Lahiri, and A. Agarwal, "Carbon nanotube reinforced metal matrix composites—A review," *Int. Mater. Rev.*, vol. 55, pp. 41–64, 2010.
[8] X. Kang, Z. M. Mai, X. Zou, P. Cai, and J. Mo, "A sensitive nonenzymatic glucose sensor in alkaline media with a copper nanocluster/multiwall carbon nanotube-modified glassy carbon electrode," *Anal. Biochem.*, vol. 363, pp. 143–150, 2007.
[9] N. Ferrer-Anglada, V. Gomis, Z. El-Hachemi, U. D. Weglikovska, and S. Roth, "Carbon nanotube based composites for electronic application: CNT-conducting polymers, CNT-Cu," *Phys. Status Solidi (a)*, vol. 203, pp. 1082–1087, 2006.
[10] B. Prevo and O. Velev, "Controlled, rapid deposition of structured coatings from micro- and nanoparticle suspensions," *Langmuir*, vol. 20, pp. 2099–2107, 2004.
[11] F. Ren, L. Yin, S. Wang, A. A. Volinsky, and B. Tian, "Cyanide-free silver electroplating process in thiosulfate bath and microstructure analysis of Ag coatings," *Trans. Nonferrous Metals Soc. China*, vol. 23, pp. 3822–3828, 2013.
[12] S. Berger and G. Hoffacker, "Novel and innovative non-cyanide silver process: A report on commercial plating experiences," *Plating Surface Finishing*, vol. 92, no. 3, pp. 46–51, 2005.
[13] N. Fishelson, A. Inberg, N. Croitoru, and Y. Shacham-Diamand, "Highly corrosion resistant bright silver metallization deposited from a neutral cyanide-free solution," *Microelectron. Eng.*, vol. 92, pp. 126–129, 2012.
[14] J. B. Mohler, *Electroplating and Related Processes*. New York, NY, USA: Chemical, 1969.
[15] M. S. Dresselhaus, G. Dresselhaus, and P. C. Eklund, *Science of Fullerenes and Carbon Nanotubes*. New York, NY, USA: Academic, 1996.
[16] R. Saito, M. S. Dresselhaus, and G. Dresselhaus, *Physical Properties of Carbon Nanotubes*. London, U.K.: Imperial College Press, 1998.
[17] J. L. Bahr and J. M. Tour, "Covalent chemistry of single-walled carbon nanotubes," *Mater. Chem.*, vol. 12, no. 7, pp. 1952–1958, 2002.
[18] S. B. Sinnott, "Chemical functionalization of carbon nanotubes," *J. Nanosci. Nanotechnol.*, vol. 2, no. 2, pp. 113–123, 2002.
[19] J. L. Stevens *et al.*, "Sidewall amino-functionalization of single-walled carbon nanotubes through fluorination and subsequent reactions with terminal diamines," *Nano Lett.*, vol. 3, no. 3, pp. 331–336, 2003.
[20] Y. P. Sun, K. F. Fu, Y. Lin, and W. J. Huang, "Functionalized carbon nanotubes: Properties and applications," *Acc. Chem. Res.*, vol. 35, no. 12, pp. 1096–1104, 2002.
[21] T. Ramanathan, F. T. Fisher, R. S. Ruoff, and L. C. Brinson, "Amino-functionalized carbon nanotubes for binding to polymers and biological systems," *Chem. Mater.*, vol. 17, pp. 1290–1295, 2005.
[22] S. Osswald, M. Havel, and Y. Gogotsi, "Monitoring oxidation of multi-walled carbon nanotubes by Raman spectroscopy," *J. Raman Spectrosc.*, vol. 38, pp. 728–736, 2007.
[23] W. Callister and D. Rethwisch, *Materials Science and Engineering An Introduction*, Appendix B, 8th *ed.* Hoboken, NJ, USA: Wiley, 2010.
[24] M. M. J. Treacy, T. W. Ebbesen, and J. M. Gibson, "Exceptionally high young's modulus observed for individual carbon nanotubes," *Nature*, vol. 381, pp. 768–680, 1996.

Authors' photographs and biographies not available at the time of publication.